Applied Physics, Material Sciences, and Engineering Journal
ISSN 3065-1425
Volume 13 Issue 2
April-June 2025
Impact Factor: 8.13
Enquiry: contact@continentalpub.online
Published by Continental Publication | https://cspjournals.org/index.php/apmsej

DYNAMIC LIMITS TO SHOCK-INDUCED BEHAVIOR IN HIGH-PRESSURE ENVIRONMENTS

Isabella Mae Thornton
The University of Manchester at Harwell, Diamond Light Source, Harwell Campus, Didcot,
Oxfordshire OX11 0DE, United Kingdom

Abstract: *Materials subjected to extreme shock compression experience a sequence of distinct regimes, each governed by different underlying physical mechanisms. This paper explores these transitions, beginning at the weak shock limit (WSL), where ambient shear strength is exceeded. Beyond the WSL, increasing strain forces electrons into progressively higher energy states. Upon reaching the shock melting pressure and beyond, materials undergo structural changes that culminate at the strong shock limit. At this point—approximately three times the melting pressure—electronic contributions dominate the material response, leading to reduced compressibility and the onset of electron degeneracy pressure. A theoretical model is presented to quantify this transition, showing that the threshold pressure depends on the free electron density. The findings highlight a critical relationship between ambient material properties and the nonlinear compression behavior under shock. This work underscores the importance of incorporating pressure-dependent physics into high-strain material models.*

Keywords: *Shock compression, Electron degeneracy, Weak shock limit, High-pressure physics*

I. INTRODUCTION

Materials under high-pressure loading exhibit sequential phases of microstructural reorganization to accommodate the imposed strain. At extreme pressures, emergent forces arising from quantum effects can lead to changes in compressibility.[1] Prior research identified a critical threshold, where the compression and eventual removal of volume defects resulted in the material achieving its ambient theoretical maximum density.[2] Beyond this threshold, the shear component of the applied stress exceeds the theoretical strength of the material. Here, homogeneous flow was observed at the meso- and greater scales in the shocked material. The transition stress, marking the end of weak shock behavior, was designated as the weak shock limit (WSL).[3,4] Other studies have explored the high-pressure behavior of solids under quasistatic and quasi-isentropic loading to extreme conditions. While these findings are relevant to the observations presented here, these states are different, and the focus of the following discussion will concern adiabatic shock loading as one limit in these states. In this regime, there are three broad regimes of behavior with thresholds described below.

The first of these is the weak shock limit (WSL) that occurs when the shock wave velocity (U_S) reaches the longitudinal wave speed in the medium (c_L) and allows the stress threshold to be derived from the condition $U_S = c_L$. The relationship between shock velocity and particle velocity (u_p), that results from the driving piston, provides critical insights into material response under dynamic loading. While many materials exhibit a linear U_S–u_p relationship, certain cases demonstrate more complex behavior requiring higher order polynomial functions in u_p for accurate characterization (refer to Table 17.1 in Ref. 5 for instance). It has been shown that at stresses above the WSL, the strong shock regime, flow is hydrodynamic, and this will be assumed in what follows here.[3] For clarity, hydrodynamic behavior refers to the response of a material under pressures that significantly exceed its shear strength, causing it to behave in a fluid-like manner, and with its response governed primarily by density and compressibility rather than solid-state mechanical properties.

In other works, it has been shown that elements above the WSL and in the strong shock regime, generally show shock wave speed U_S that follow a linear function of the particle velocity u_p expressed as

U_S ¼ c_o þ Su_p, (1)

where U_S is the shock front speed; u_p the particle velocity behind it; c_o the zero-pressure bulk sound speed until thermodynamic phase transitions occur.[3] The constants c_o and S are most commonly fitted to shock data and in some cases higher order fits are used to capture more complex behaviors.[5–7] This procedure was first introduced by Rice et al. to generate data for a series of metals.[8,9] However, many solids in the weak shock regime show more complex responses. Kerley proposed a more sensitive analysis to reveal thresholds, transforming the ordinate from U_S to $U_F = U_S - u_p$.[10] The strong shock regime, best seen by plotting the shock velocity U_F vs the particle velocity u_p, shows remarkably linearity in many materials and has a slope generally different from that in the weak shock regime.[3] The transformation defines

U_F ¼ U_S u_p ¼ c_o þ (S 1)u_p, (2)

where U_F can be thought of as the velocity at which the shock front outruns the driving piston (see Ref. 10). U_F represents shock velocity in a frame of reference moving with the material behind the shock at velocity u_p and is a useful transformation to isolate critical thresholds and probe regions of linear response.

In the strong shock regime, subsequent deformation involves ionic displacement against repulsive interatomic potentials. This phase is generally characterized in metals by electronic bands converging, while their bandgap widens and with their energy rising with increasing strain. The transition from mesoscale deformation around volumetric defects (weak shock region) to microscale compression at the atomic scale induces consequent electromagnetic phenomena as the threshold is crossed. The weak shock regime terminates at the point where shock velocity equals the elastic wave speed and is indicated by blue markers in the following figures. The experimental data presented are derived from shock compendia that have aggregated information from various experimental platforms over several decades. Given the diverse origins and extended timeframe of data collection, assigning precise error bars to each dataset is not feasible. Nevertheless, the trends are still clear regardless of this, as will be seen in what follows.[5,7,8]

At the WSL point,

U_S^{WSL} ¼ $c_L$which implies u^{WSL}_p ¼ (c_L c_o)/S: (3)

Beyond this value, as shocks lie in the strong shock regime, the data exhibit a linear region (shown in green) that extends to a threshold characterized by a change in slope, before then transitioning to regime where the curve exhibits a lower gradient and greater compressibility at higher pressures and shown in red. While metallic materials generally do not display remarkable electromagnetic behaviors at this threshold, non-metallic and ionic solids demonstrate a range of phenomena. For example, the ionic solid KCl undergoes an insulator-to-conductor transition, piezoelectric materials like quartz exhibit luminescence, and explosives display accelerated reaction kinetics beyond this critical point.[4,11,12]

II. SOLIDS AT HIGH COMPRESSION

To observe these regimes, consider behavior observed at the limits of strong shock behavior, in the most studied of the metals, aluminum, and the widely used ionic, window material, single crystal lithium fluoride. The latter has a large bandgap which means that its crystals are more transparent to short wavelength radiation than any other substance, thus providing a material for backing targets for interferometry that is transparent over a wide range of pressures on the rear of shocked targets. Its impedance is also close to that of aluminum, which makes it a versatile standard for use in a range of experiments using VISAR and PDV.[13,14] The mechanical response under shock for LiF has thus been extensively probed, alongside changes in refractive index with compression that occur in the loading to the threshold at the end of strong shock behaviors.[15–18]

The response of aluminum [Fig. 1(a)] has a change in slope which corresponds to the Weak Shock Limit at the condition $U_S = c_L$. The corresponding threshold in the plot corresponds to a reduced shock velocity, $U^{WSL}{}_F = c_L-(c_L - c_o)/S$, where c_o and S refer to the constants derived for the response in the strong shock regime (between the WSL and the SSL). The WSL is crossed at a compressive strain of around 13%. There is a further change in slope at a particle velocity around the sound speed of aluminum, $u_p = c_L$, that corresponds to a compressive strain of around 46 %. This threshold marks the end of the strong shock regime and is a further higher transition in behavior for the material. It is, thus, labeled the strong shock limit (SSL) in what follows. Between, the two materials show melting under shock loading and this typically occurs at around a third of the pressure at the SSL. There is no significant change of slope observed in U_F–u_p plots at this threshold as will be seen below.

Beyond this point, the solid becomes more compressible with increasing pressure, suggesting changes in its electronic state. Additionally, above this threshold, greater data scatter is observed due to the challenges of obtaining reliable measurements at such high pressures. In the case of LiF [Fig. 1(b)], there are fewer data points available for experiments published above the transition. However, it is still possible to infer a reduction in the value of S. This occurs at a compressive strain of around 47%. Further, there are changes in electromagnetic properties observed at these compressions—in the case of the LiF window there is a reduction in transmission until an abrupt loss of beam intensity and a total loss of fringe information occurs at stress levels of between 220 and 240 GPa.[16]

The transition at the SSL is observed consistently across a range of materials for which empirical data are available. However, the number of materials with significant data at these high pressures is constrained due to the challenge of generating the extreme states required to elevate the particle velocity beyond the ambient elastic wavespeed and the difficulties of data acquisition in this extreme regime. This limitation may, to some extent, reflect the novel electronic states that manifest in this regime. Figure 2 illustrates the response of elements Bi, Fe, Cu, and Sn. The datasets for Fe and Cu are comprehensive, spanning an extensive pressure range, yet all exhibit the high-pressure threshold that is the focus of this study.[20–30] The weak shock, strong shock, and post-SSL regimes are demarcated in blue, green, and red, respectively, in each plot. These materials have been extensively investigated and

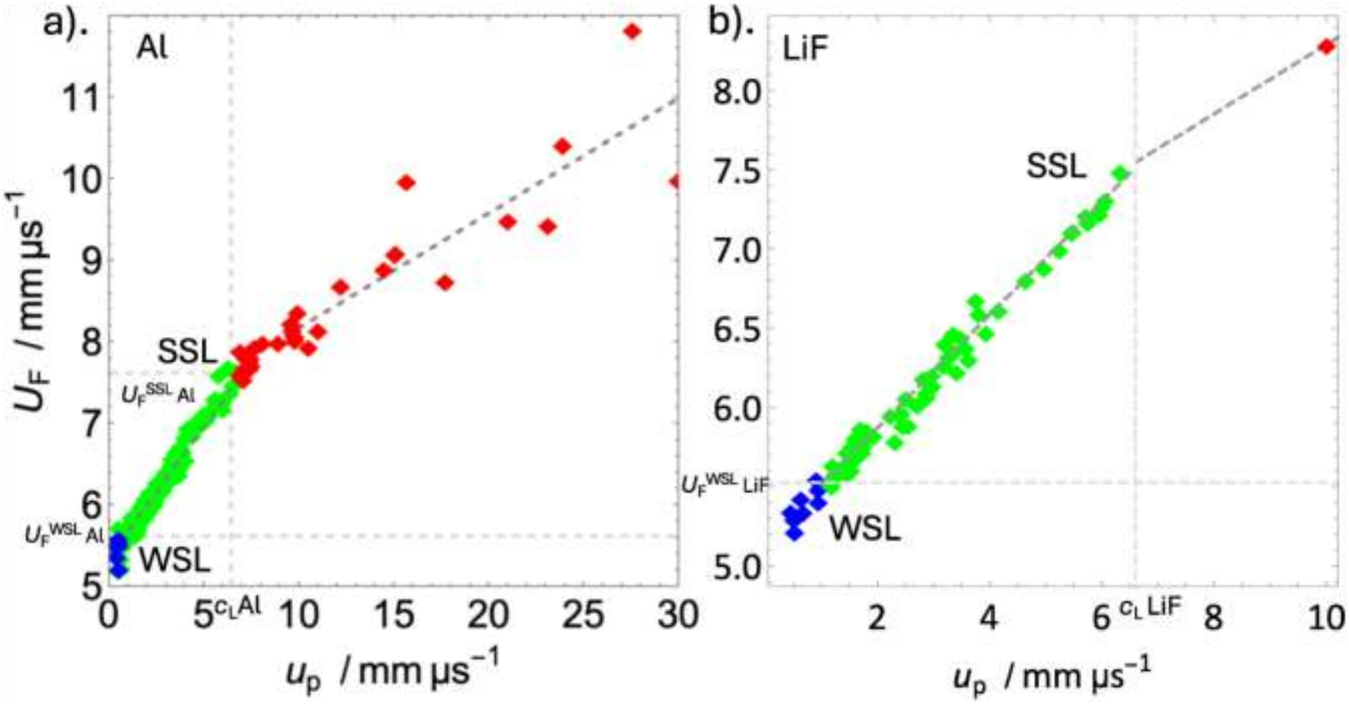

FIG. 1. U_F–u_p response of Al and LiF showing data from Refs. 6, 7, 18, and 19. The horizontal lines correspond to the point, U_F^{WSL}, defined below, the reduced shock wave speed for the material. The vertical lines are at the positions where $u_p = c_L$. These are the conditions for the weak and strong shock limits for the material, the lower intersection is the WSL, and the upper corresponds to the SSL.

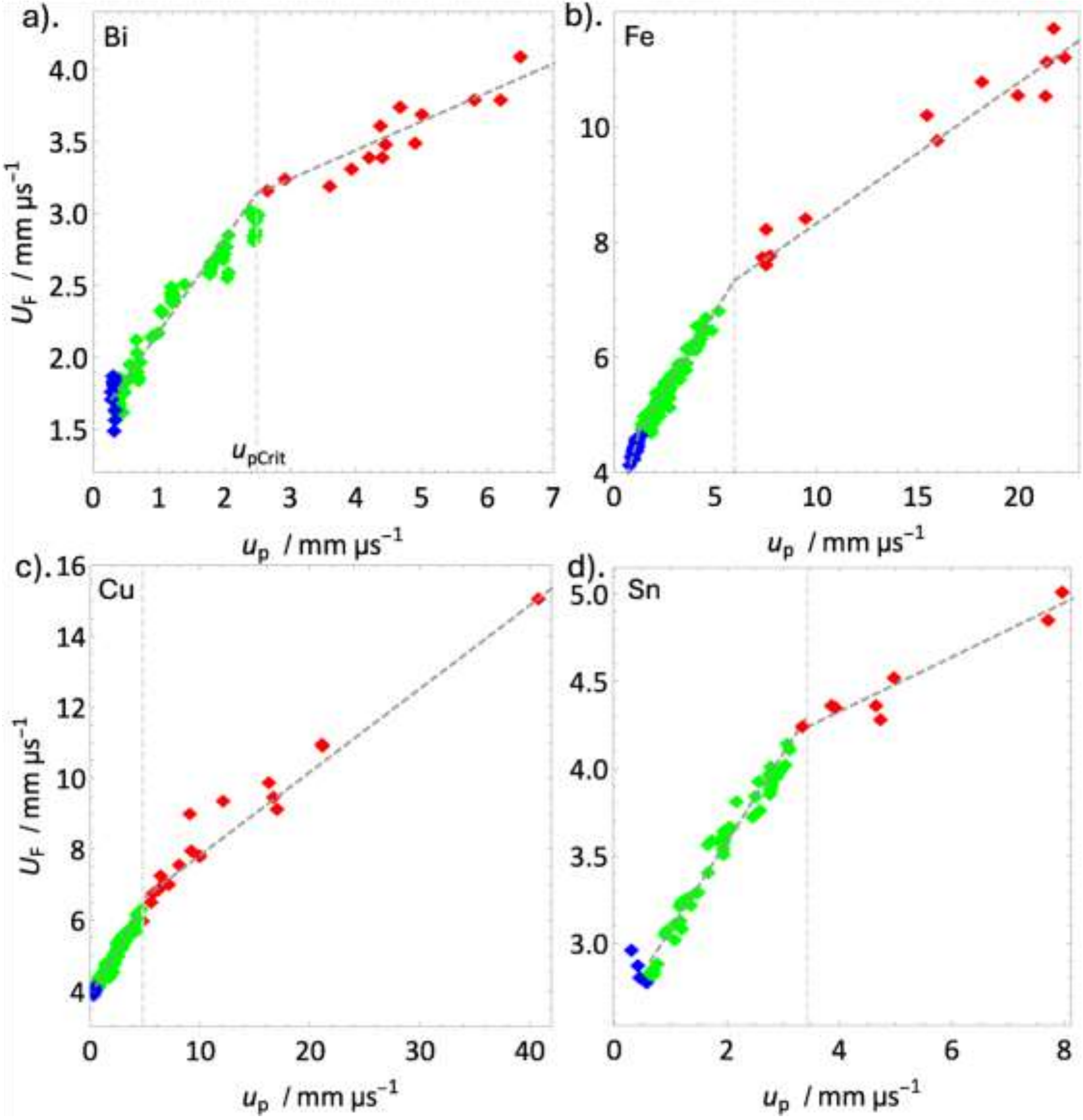

demonstrate martensitic phase transitions in the lower-pressure regime, with each exhibiting a subsequent shift in behavior at a higher threshold. For bismuth, shockinduced transitions are reported at 2.7, 3.2, and 7.0 GPa, with melting occurring between 17 and 27 GPa under laser shock loading.[31–34] The martensitic phase transition in iron is well-documented (see Refs. 28 and 35 for reference), and a high-pressure transformation to the BCC structure in copper is observed at 180 GPa.[36,37] Tin exhibits a shock-induced β-bct transition at 9–10 GPa.[38,39] These transitions occur at lower thresholds than the higher-pressure transformations that manifest at critical particle velocities u_{pCrit}. Beyond this point, all these materials demonstrate significantly increased compressibility and S is reduced.

It is important to correlate the magnitude of thresholds with existing physical constants for the materials. Given that the modulus reflects a substance's resistance to compression, a transition point may be anticipated, reflected in the bulk and longitudinal wave speeds, as previously suggested.[40,41] Consequently, for the range of materials analyzed, the particle velocity at the transition point, u_{pCrit}, was

FIG. 2. Reduced shock velocity vs particle velocity for elements (a) Bi, (b) Fe, (c) Cu, and (d) Sn. The weak shock regime is again plotted with blue coloring, the strong shock in green, and the state beyond where compressibility increases, in red. Fits to the strong shock data and that beyond are shown with an intersection at u_{pCrit} for each material [shown in (a)]. The condition $u_p = c_L$ is plotted as a vertical dashed line for each material.

evaluated and tabulated against the values of the bulk and longitudinal wave speeds at ambient pressure, derived from fits to behavior in the strong shock regime.[3] These data, along with constants for each material, are presented in Table I. Plotting these quantities against the respective wave speeds at 300 K (Table I) reveals a linear dependence for both c_0 and c_L (Fig. 3). Here, c_0 is taken from data fitted in the strong shock regime.[3] Of course, the longitudinal elastic wave speed varies with temperature, and thus ideally, a comparison with measured values for the sound speed interpolated to absolute zero would be preferable. However, for reference, the elastic constants for aluminium measured at room temperature and zero kelvin, coupled with changes in density over the same range, yield a variation in wave speed of only 3%. This systematic error, applicable to all plotted metals here, is not considered significant given the errors introduced by estimating the critical cut-off velocity. The errors in u_{pCrit} result from the availability of high-pressure data, gathered in states above the SSL. The range of metals where an accurate value can be determined is limited given paucity of data in these extreme conditions.

This representation of the data using reduced shock velocity is crucial in this analysis, as it highlights breaks in slope more distinctly than conventional U_S–u_p plots. Figure 3 clearly demonstrates that the best fit to the data reveals a 1:1 relationship between the critical velocity and the ambient longitudinal wave speed of the material. In contrast, Johnson's previous work compared the critical velocity to the bulk sound speed c_0 and identified a break in slope occurring at $u_{pCrit} = 1.6c_0$.[43] The correlation with longitudinal sound speed is unexpected at these extreme pressures. This observation raises interesting questions about the behavior of materials under such intense conditions and suggests that the importance of moduli persist to this extreme state.

At the SSL, the material with initial density, ρ_0, is in a state where the particle velocity, u^{SSL}_p and the shock velocity U^{SSL}_S can be substituted to calculate the pressure P^{SSL}, thus if u^{SSL}_p ¼ c_L at the SSL, this implies P^{SSL} ¼ $\rho_0(c_0$ þ $S\ c_L)c_L$: (4)

In the metal aluminum shown in first example above, this corresponds to a pressure of 239 GPa while in the window material lithium fluoride, the threshold correlates with the loss in transparency at 245 GPa. The mean strain calculated at this pressure (u^{SSL}_p / U^{SSL}_S) is 0.46 for aluminum and interestingly also for LiF. At the two thresholds discussed (the WSL and the SSL), the mean strain for the materials discussed is 0.16 at the WSL and 0.45 at the SSL. It is surprising there is such consistency across these metals for these values at these thresholds given the differing potential wells for each material, however it does point to a consistency in behavior across the strong shock regime that is reflected in the response of the metals presented.

III.

TABLE I. Data for all elements analyzed giving values of u_{pCrit} at the point of the change in slope, for elements Al, Bi, Cd, Cu, Fe, Mo, Pb, Sn, Ta, Zn. Density, ρ_0, Strong shock constants, c_0 and S in the strong shock regime, elastic and shear wave speeds c_L and c_S, the weak shock limit, σ_{WSL} (taken from Ref. 3), critical velocity for strong shock threshold u_{pCrit}, pressure at this threshold P_{Crit} calculated using u_{pCrit} with its associated errors, and shock constant, S_{Crit} that is indicative of compressibility in the regime beyond the strong shock limit. Constants and values of strong shock constants taken from Refs. 3 and 42.

	ρ_0/g cm^{-3}	c_0/mm μs^{-1}	S	c_L/mm μs^{-1}	c_S/mm μs^{-1}	σ_{WSL} (GPa)	upCrit/mm μs^{-1}	P_{Crit} (GPa)	SCrit
Al	2.70	5.38	1.32	6.40	3.15	13.3	6.5 ± 0.7	240 ± 40	1.19 ± 0.02
Bi	9.78	2.14	1.31	2.49	1.43	6.5	2.6 ± 0.1	132 ± 8	1.20 ± 0.04
Cd	8.64	2.46	1.30	3.14	1.67	32.8	3.1 ± 0.3	200 ± 30	1.23 ± 0.02
Cu	8.93	3.90	1.51	4.76	2.33	24.2	4.8 ± 0.5	470 ± 80	1.23 ± 0.02
Fe	7.85	4.60	1.58	5.94	3.26	58.1	5.7 ± 0.9	600 ± 200	1.24 ± 0.02
Mo	10.20	5.14	1.26	6.48	3.35	69.8	6 ± 2	900 ± 200	1.22 ± 0.05
Pb	11.40	2.05	1.47	2.25	0.89	1.8	2.5 ± 0.2	130 ± 20	1.18 ± 0.01
Sn	9.29	2.47	1.51	3.43	1.77	15.9	3.2 ± 0.4	200 ± 40	1.16 ± 0.05
Ta	16.60	3.28	1.31	4.14	2.03	45.3	4.0 ± 0.2	600 ± 50	1.3 ± 0.2
Zn	7.14	3.12	1.49	4.07	2.35	18.5	4 ± 1	300 ± 100	1.3 ± 0.1

DISCUSSION—POTENTIAL BEHAVIORS AT HIGH PRESSURES

DOI: https://doi.org/10.5281/zenodo.15845931

The simple plots of experimental shock velocity vs corresponding particle velocity behind the shock front contain a

DOI: https://doi.org/10.5281/zenodo.15845931

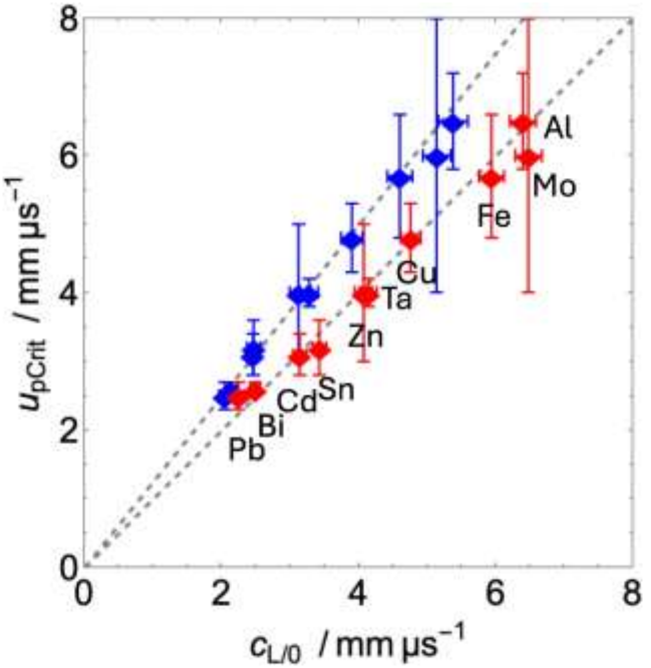

FIG. 3. Measured particle velocity at the exit of the strong shock regime, u $_{pCrit}$, for elements Al, Bi, Cd, Ce, Cu, Fe, Mo, Pb, Sn, Ta, Zn plotted vs velocities of bulk (c_0 in blue) and longitudinal waves (c_L—measured at 300 K—in red). The 1:1 correlation between the critical particle velocity and the longitudinal wave speed reflects the dependence of behavior best. The datasets vary in the number of points that affects errors determining the position of changes in slope, but a typical error is shown for the data. The slopes of the best fit curve to each dataset are $u_{pCrit} = 1.23c_0$ and $u_{pCrit} = 0.99c_L$.

wealth of information. The flow speed is a function of both the material's modulus and density, reflecting the electronic bonding within the lattice and the atomic number of the compressed element, respectively. Consequently, wave speeds provide an integrated ranking of the behavior of solids under load. The thresholds observed here correspond to distinct regimes of behavior, each dominated by different predominant forces governing the material's response. These relationships offer insight into the complex interplay between a material's atomic structure and its dynamic response to compression. Compression of condensed matter proceeds through a series of stages, each delineated by distinct thresholds marking changes in mechanisms accommodating the applied strain. The initial stage involves the compaction of elemental assemblages into a cohesive structure capable of supporting stresses through the strength of interconnected components. Beyond this, a regime exists where further compaction remains reversible upon unloading due to elastic behavior within the elements. A subsequent threshold is crossed when strain concentration around volume defects enables solid densification through localized collapse and irreversible compaction. In this phase, temperature increase across the shock front is minimal (although of course positive) and localized at mesoscale hot sites within the flow. This weak shock regime exhibits non-linear behavior, transitioning from defect-dominated flow at the mesoscale, to atomic-scale compression beyond theoretical maximum density (TMD), signaling the onset of the strong shock regime. Beyond this weak shock limit, all volume defects in the material are eliminated, resulting in a flow homogenized at the mesoscale behind the shock front. Using the relation from (3), this threshold stress at the WSL can be simply written as

σWSL ¼ρ0USWSLuWSLp ¼ρ0cL(cL c0)/S: (5)

Beyond the weak shock limit, compression is governed by strong electrostatic forces as ions are forced into closer proximity. This intense compression induces profound changes in the material's electronic structure.

As compression progresses, the lattice's shear strength diminishes until it reaches a critical strain at which strength is lost entirely across a range from start to completion of melt of pressures of order 10 GPa. This phenomenon is conventionally termed "shock melting" and can be experimentally determined by measuring the disappearance of the elastic release component from the highpressure shock state or tracking the transition using diffraction experiments.[44] Clearly, the transition to this shock-melted state marks the point where the material's crystalline structure breaks down, and begins to exhibit fluid-like properties. This transition is crucial for understanding material behavior in high-energy impact scenarios, planetary interiors, and other extreme environments. The ability to predict and measure shock melting is vital for various scientific and engineering applications, including the design of protective armors, the study of planetary formation, and the development of new materials for extreme conditions.

The seminal research of Walsh and Christian established foundational methodologies for temperature calculations, which, when combined with Ross's adaptations of the Lindemann melting criterion, enable quantitative predictions of shock-induced melting thresholds.[45–47] This theoretical framework has been supported with experimental measurements across the various metallic systems discussed above.[34,48–53] Melting pressures, P_{melt}, were calculated for the metals in this work and the ratio of these to the pressure at the strong shock limits, P_{SSL} is shown in Fig. 4. The data indicate that melting typically initiates at pressures between 0.2 and 0.5 times that at the strong shock limit (SSL), with a characteristic value of approximately 0.35 P_{SSL} for the metals included. Melting thus

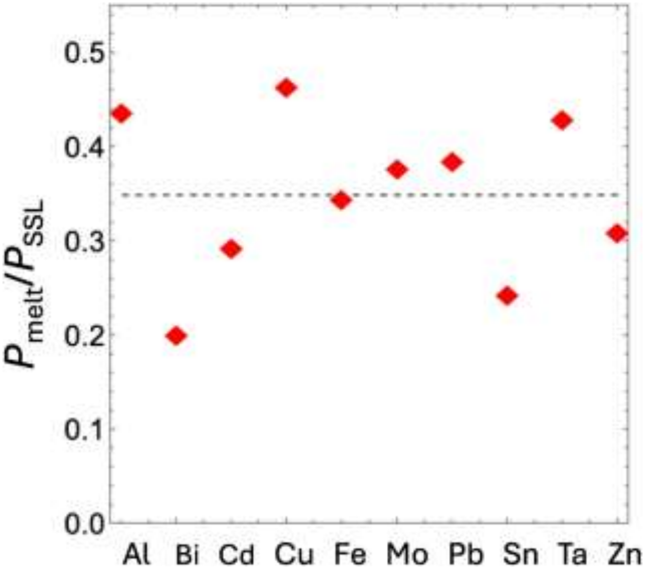

FIG. 4. Variation of the calculated pressure at first melt divided by the pressure at the strong shock limit, P_{melt}/P_{SSL}, for the metals discussed. The mean value for these metals at 0.35 is plotted as a dotted line. The calculated and measured pressures will have some error in the region of 5%, but the general trend shows that shock melt occurs at a fraction of the pressure at the SSL.

occurs substantially before the SSL and the observations presented for behavior at these much higher pressures are not thermal in origin. Indeed at these substantially higher pressures, between 2 and 4 times the melt pressure, materials transition to a quantum state where behavior becomes temperature-independent, as discussed for quantum melting in pressure-ionized systems and in the response of dense materials like vanadium.[54,55]

As materials experience further compression, several significant changes occur in their electronic structure. Increased electron density and the overlap of electronic orbitals lead to the formation of new electronic states and band broadening. At extreme pressures, core electrons can become involved in bonding or delocalization. Further, as pressure increases, energy levels generally tend to move closer together due to orbital compression and changes in interatomic potentials. This process encourages distinct energy levels to merge, as degenerate electron states approach one another and interband gaps decrease, potentially leading to metallization or other novel electronic states. These behaviors result in a range of observable phenomena, including increased conductivity or transition from insulators to metals due to pressure-induced band overlap, and in some cases, superconductivity may emerge as electron pairing mechanisms change.[56] Lithium fluoride, presented above, serves as a notable example of these effects. Typically, an ionic insulator under ambient conditions, it exhibits significant electronic changes under high pressures. These include the closure of bandgaps with increasing pressure, leading to metallization when the conduction and valence bands overlap. Furthermore, the proximity of ions under high pressures facilitates hybridization between lithium and fluoride orbitals, creating new states with unique electronic properties and potential degeneracies. Understanding these pressure-induced changes is crucial for predicting material behavior in extreme environments and for advancing applications in high-pressure physics, materials science, and planetary science.

It is hypothesized that the strong shock limit represents the threshold defined by the degeneracy pressure exerted by free electrons. This pressure arises from two fundamental quantum mechanical tenets: the Pauli exclusion principle and the Heisenberg uncertainty principle.[57] Momentum conservation equates the force to the rate of change of momentum across the shock. Thus, if P is the pressure across the front and ρ_1 and ρ_0 are the densities either side of it, then $P = \rho_0 U_s u_p$ that, with the conservation of mass equation, $\rho_0 U_s = \rho_1 (U_s - u_p)$, implies that[40]

$P\ ¼\rho_0\rho_1 u^2_p/(\rho_1\ \rho_0)$:

This may be expressed in terms of the volumetric strain, $\varepsilon = u_p/U_s = 1 - \rho_0/\rho_1$, to give

$P\varepsilon\ ¼\rho_0 u^2_p$,

which is a simple statement that work done on the solid equates to the increase in kinetic energy in it, and which, at the SSL where $u_p = c_L$, implies

$PSSL\ ¼\rho 0c2L/\varepsilon crit\ ¼\ (K\ þ\ 4/3\mu)/\varepsilon crit$, (6)

where the bulk and shear moduli (K and μ) are evaluated at the ambient state and ecrit is the strain at the SSL. If the stiffness was governed exclusively by electronic properties—specifically, the energy difference between the ground state of the valence electrons and the corresponding state in a uniform electron gas—then this condition would represent the direct input of that energy into kinetic energy in the system. We can thus calculate the pressure at the SSL, assuming only that the moduli need to be determined and these may be compared with the measured state at the critical strain to demonstrate the relation. The work done on the system comprises two components: compression of the atomic electron cloud, which is governed by the bulk modulus, and collapse of the packed ionic structure, which is determined by the shear modulus and in what follows, the quantity $K_{SSL} + 4/3\ \mu_{SSL}$ at the SSL is referred to as the degeneracy modulus at this pressure.

To determine the bulk modulus and calculate the degeneracy pressure, free electron theory can be used to provide estimates that can be compared to the measured critical points at which the compressibility (S) changes. However, the free electron model (FEM) makes the key assumption that the number of conduction electrons per atom is dictated by the valence of the element. It does not account for crystal structure and neglects electron ion interactions so works best for alkali and noble metals. Further, it is known to be inaccurate for transition metals. To validate these assumptions at the SSL (where $u_p = c_L$), the bulk modulus may be calculated using the FEM. It is well known that a component of the bulk modulus K can be ascribed to quantum confinement at high pressure and the stiffness can be represented in terms of the free electron density ρ_e. Thus,

$$K_{FEM} = \frac{2}{3}\left(3\pi^2\right)^{2/3}\frac{h^2}{2m_e}\rho_e^{5/3}, \quad (7)$$

where h is Planck's constant divided by 2π and m_e is the mass of an electron.[58] The valence electron number density, ρ_e, is generally lower than that tabulated in handbooks. Here, the methods of Lang are used to introduce more realistic values by considering the quantum behavior of conduction electrons, and their response to lattice distortions since this allows a more precise prediction of the elastic properties of metals under deformation.[59] The FEM has a dependence of the electron density that scales as the applied strain to the power 5/3 since electron density is assumed to scale as mass density at these pressures. Thus, the degeneracy modulus and the calculated pressure at the SSL can be derived from (6) for the ten metals discussed in this work.

The results of the degeneracy moduli calculations derived using this approach are presented in Table II, alongside the corresponding degeneracy pressure ($P_{FEM} = 3/5\ K_{FEM}$). Also listed are the experimental thresholds discussed earlier, including the critical strain at the SSL, ε_{Crit}, the corresponding pressure P_{SSL}, and the calculated equivalent transition pressures obtained using the degeneracy moduli and the critical strain. Given the known limitations of the free-electron model and the variation in crystal stacking among metals, a second calculation is included for comparison. This uses the measured ambient moduli (derived from elastic wave speeds) scaled by ε_{crit} to account for pressure effects. As a validation, the bulk modulus under ambient conditions was also computed using the FEM. While the calculated bulk modulus aligns with the expected order of magnitude, it does not match the experimental value, highlighting the model's deficiencies in the ambient state. These discrepancies arise because the free-electron model neglects microstructural effects, as well as electron–electron and electron–ion interactions. Consequently, the predicted ambient pressure is generally inaccurate.

However, at the strong shock limit, the calculated pressures show better agreement with experimental data, which validates the hypothesis that electrons are free at this threshold.

The values for the calculated pressures, P_{FEM}, and those measured at the SSL, P_{SSL}, are plotted in Fig. 5. The calculated points using the FEM [Eq. (7)], plotted in red, show scatter around the 1:1 guide plotted. Two data points corresponding to Mo and Ta, that retain their BCC structure at high pressures (shown in orange), deviate from the trend line and have predicted pressures that are too low. This highlights limitations in the model's ability to accurately capture structural behavior. Nevertheless, this

TABLE II. Data for all elements analyzed, giving quantities at the point of change in slope, u_{pCrit}, for elements Al, Bi, Cd, Cu, Fe, Mo, Pb, Sn, Ta, and Zn. Values are presented for the mass density, ρ_o, the valence electron density, ρ_e, the calculated bulk modulus from FEM, K_{Th}, the experimentally measured bulk modulus, K_{Exp}, the calculated degeneracy pressure, P_{Degen} and the measured pressure at the strong shock limit, P_{SSL} and the critical strain at the transition to lower compressibility at the SSL, ε_{Crit}. Values for calculated degeneracy modulus [derived from Eq. (6)] and the measured moduli scaled by ε_{Crit} are tabulated.

	ρ_o/g (cm^{-3})	ρ_e × 1028 (m−3)	K_{Th} (GPa)	K_{Exp} (GPa)	P_{Degen} (GPa)	P_{SSL} (GPa)	εCrit	P_{FEM} (GPa)	P_{Exp} (GPa)
Al	2.70	12.1	114	78	69	239	0.47	267	245
Bi	9.78	2.82	10	45	6	132	0.47	73	151
Cd	8.64	9.31	74	95	45	211	0.42	208	302
Cu	8.93	17.0	203	135	122	471	0.43	505	465
Fe	7.85	17.0	203	124	122	623	0.44	604	535
Mo	10.20	14.8	161	270	97	878	0.48	576	872
Pb	11.40	13.2	133	48	80	128	0.44	259	136
Sn	9.29	6.6	42	45	25	191	0.44	142	172
Ta	16.60	5.6	31	179	19	600	0.46	248	579
Zn	7.14	12.4	120	69	72	267	0.44	329	280

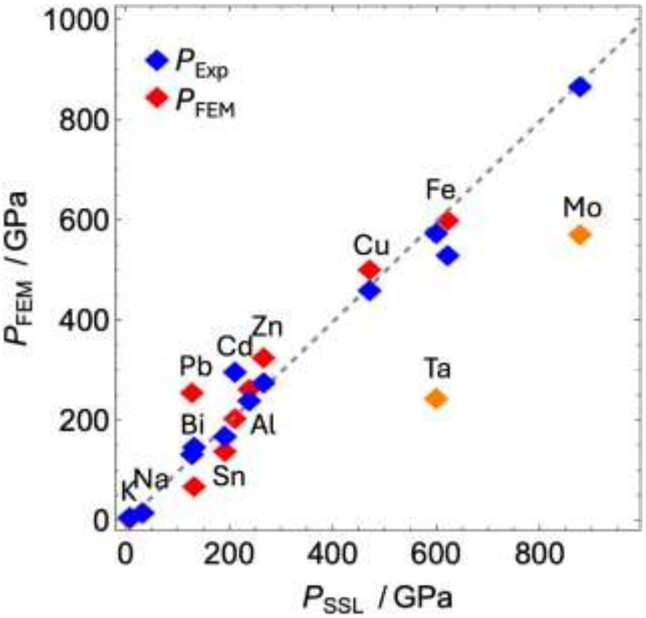

FIG. 5. P_{FEM} calculated using FEM theory (in red) and by scaling measured moduli (P_{Exp} in blue) plotted against P_{SSL}, calculated from the values for u_{pcrit} and using Eqs. (4) and (7). The dotted line represents 1:1 correspondence. Two points, for Mo and Ta (plotted in orange), lie away from the best fit line.

simplified model effectively reproduces the data on these metals and supports assumptions regarding the proximity of this state to the metal's degeneracy pressure. For comparison, ambient experimental values for moduli, simply corrected for strain (as discussed above), closely align with high-pressure behavior (shown in blue).

This suggests that in shock compression to the SSL pressure, the kinetic energy of the shock wave is expended overcoming resistance from valence bonds reflected in the material's elastic and electronic moduli, which are both functions of electron density. As pressure increases, electron density approaches a critical threshold where delocalization occurs, that directly influences the material's equation of state. This behavior can be described using theories such as the Mott transition model, where delocalization of bound electrons occurs when the interatomic spacing reaches a critical value.[60]

This correlation suggests that ambient material moduli govern material compression up to nearly 50% strain. Beyond this value, alternative electronic arrangements change material behavior aligning with the hypothesis that beyond the strong shock limit, ions sit within a degenerate electron gas. Further, in this region degeneracy pressure remains largely independent of temperature—a key characteristic of degenerate matter.

Ashworth's work calculating quantum states at these extreme pressures provides further insight into this regime. He reports that valence electrons localize in interstitial regions away from ions, while bandwidth appears to decrease monotonically.[61] These observations highlight the complex interplay between atomic structure, electronic behavior, and material properties under extreme conditions. Johnson has discussed the state of matter in the region up to and beyond the strong shock limit.[43,62,63] Further, his work derives an expression for the value of constants at higher compressions, assuming electronic thermal excitations begin to dominate, and electron ionization occurs. In Johnson's model,

S_{Crit} asymptotes to 1.2 in this state, providing a hypothesis for the observed break in slope and high-pressure linearity. However, there is a scarcity of data available above the SSL, and many uncertainties exist in the analysis at these extreme pressures, making it challenging to fit behavior with certainty. The most accurately determined state measurements, derived from nuclear-explosive-driven experiments, have been used to obtain equation of state (EOS) data at extremely high pressures, sometimes with ±2% accuracy.[64] Despite this, different impedance-matching standards can result in large uncertainties in inferred states, leading to scatter in data at these levels. Nevertheless, the entries in Table I for the fitted values of S_{Crit} are distributed around 1.2, aligning with Johnson's model predictions. This distribution supports the hypothesized mechanisms of ionization occurring across this region. These correlations between theoretical predictions and experimental observations, despite the challenges in data collection and analysis, underscore the importance of continued research in this field. Further studies at these extreme pressures could provide valuable insights into the behavior of matter under conditions relevant to astrophysical phenomena and advanced materials science. The system presents a unique theoretical challenge, as it operates at the interface between classical mechanics and quantum mechanical regimes, offering promising opportunities for developments in computational approaches such as density functional theory, for instance.

IV. CLOSURE

The continuous compression of materials traverses a range of states, each characterized by distinct microstructural and electronic responses. This process begins with an elastic regime where microstructural elements deform around volume defects and progresses to a state of extreme compression where electronic states become degenerate, and ions adopt new structures. This compression range corresponds to a pressure increase of approximately 10^7 times the initial yield stress, resulting in a density nearly double that of the original material. Three key thresholds are discussed in this paper. In the lower pressure regime, compression transitions from weak to strong shock at the weak shock limit. This transition, occurring at strains around 16%, marks the achievement of the ambient theoretical maximum density. Beyond this point, ions move closer together, raising electronic energy levels, decreasing bandgaps, and reducing valence bond strength as strain and temperature increase. Shock melting, at about one third of the pressure at the SSL, lies between the weak and the strong shock limits. A second transition at the strong shock limit itself occurs at approximately 46% strain, characterized by a shift to greater compressibility as observed in experimental shock data. The particle velocity at the transition appears to correlate with the ambient elastic wave speed for a range of metals chosen since they possess sufficient high-pressure data. This state is hypothesized to correspond to the onset of electron degeneracy, generating significant pressure that resists further compression and can be derived from the free electron number density at this threshold. Beyond the SSL, material response is governed by quantum states, with vibrational temperature playing a diminished role. Electronic thermal excitations and ionization dominate, and the shock parameter S asymptotes to 1.2.[43] Thus, the weak shock limit defines the threshold beyond which no component of the mesoscale microstructure can sustain an elastic wave. The strong shock limit is that at which the material particle velocity exceeds the ambient elastic wave speed and the kinetic energy of the shock wave is expended overcoming resistance governed by the material's elastic and electronic moduli.[3,4]

The data presented, along with the derivation of the relationships between quantum and mechanical quantities at the SSL, pose a challenge to the scientific community to experimentally investigate and further refine the theoretical description of this transition. This will require the development of models that account for altered electronic states, and develop pseudopotentials for molecular dynamics simulations that reflect the changes in the dominant forces as one crosses these extreme regimes.[61]

Future progress in this field hinges on the development of new shock drivers and measurement techniques to generate accurate high-pressure data for a wider range of materials. These advances will contribute to the construction of consistent equations of state that accurately describe thermodynamic properties across solid, liquid, and plasma states, furthering our understanding of matter under extreme conditions.

ACKNOWLEDGMENTS

The author acknowledges election to the Rosen Scholarship at Los Alamos National Laboratory. The paper is released for publication under LA-UR-24-29349.

AUTHOR DECLARATIONS

Conflict of Interest

The author has no conflicts to disclose.

Author Contributions

Neil K. Bourne: Conceptualization (lead); Formal analysis (lead); Investigation (lead); Writing – original draft (lead); Writing – review & editing (lead).

DATA AVAILABILITY

Data sharing is not applicable to this article as no new data were created or analyzed in this study.

REFERENCES

Al'tshuler, L. V., Bakanova, A. A., Dudoladov, I. P., Dynin, E. A., Trunin, R. F., & Chekin, B. S. (1981). Shock adiabatic curves of metals. Journal of Applied Mechanics and Technical Physics, 22(2), 145.

Al'tshuler, L. V., Kalitkin, N. N., Kuz'mina, L. V., & Chekin, B. S. (1977). Shock adiabats for ultrahigh pressures. Soviet Physics JETP, 45, 167.

Barker, L. M., & Hollenbach, R. E. (1972). Laser interferometer for measuring high velocities of any reflecting surface. Journal of Applied Physics, 43, 4669. https://doi.org/10.1063/1.1660986

Bourne, N. K., & Townsend, D. (2000). Variations in the conductivity of shocked KCl. In M. D. Furnish, L. C. Chhabildas, & R. S. Hixson (Eds.), Shock Compression of Condensed Matter—1999 (pp. 109–112). American Institute of Physics.

Brooks, W. P. (1965). Shock-induced luminescence in quartz. Journal of Applied Physics, 36(9), 2788–2790. https://doi.org/10.1063/1.1714420

Brown, J. M., & McQueen, R. G. (1986). Phase transitions, Grüneisen parameter, and elasticity for shocked iron between 77 GPa and 400 GPa. Journal of Geophysical Research, 91, 7485–7494. https://doi.org/10.1029/JB091iB07p07485

Bushman, A. V., Lomonosov, I. V., & Khishchenko, K. V. (2002). Rusbank shock wave database. http://www.ihed.ras.ru/rusbank/

Duff, R. E., & Minshall, F. S. (1957). Investigation of a shock-induced transition in bismuth. Physical Review, 108, 1207–1212.

Fortov, V. E. (2011). Extreme states of matter: On Earth and in the cosmos. Elsevier.

Glushak, B. L., Zharkov, A. P., Zhernokletov, M. V., Ternovoi, V. Y., Filimonov, A. S., & Fortov, V. E. (1989). Experimental investigation of the thermodynamics of dense plasmas formed from metals at high energy concentrations. Soviet Physics JETP, 69, 739.

Greeff, C. W., Boettger, J. C., Graf, M. J., & Johnson, J. D. (2006). Theoretical investigation of the Cu EOS standard. Journal of Physics and Chemistry of Solids, 67, 2033–2040.

Hawreliak, J. A., Winey, J. M., Toyoda, Y., Wallace, M., & Gupta, Y. M. (2023). Shock-induced melting of [100] lithium fluoride: Sound speed and Hugoniot measurements to 230 GPa. Physical Review B, 107, 014104.

Kerley, G. I. (2006). The linear US–up relation in shock-wave physics. Kerley Technical Services Research Report. Kerley Technical Services.

Kormer, S. B., Funtikov, A. I., Ulrin, V. D., & Kolesnikova, A. N. (1962). Dynamic compression of porous metals and the equation of state with variable specific heat at high temperatures. Soviet Physics JETP, 15, 477–488.

Marsh, S. P. (1980). LASL shock Hugoniot data. University of California Press.

Nellis, W. J., Moriarty, J. A., Mitchell, A. C., Ross, M., Dandrea, R. G., Ashcroft, N. W., Holmes, N. C., & Gathers, G. R. (1988). Metals physics at ultrahigh pressure: Aluminum, copper, and lead as prototypes. Physical Review Letters, 60(13), 1414.

Rice, M. H., McQueen, R. G., & Walsh, J. M. (1958). Compression of solids by strong shock waves. In F. Seitz & D. Turnbull (Eds.), Solid State Physics (Vol. 6, pp. 1–63). Academic Press.

Rigg, P. A., Knudson, M. D., Scharff, R. J., & Hixson, R. S. (2014). Determining the refractive index of shocked [100] lithium fluoride to the limit of transmissibility. Journal of Applied Physics, 116, 033515.

Romain, J. P. (1974). Phase transformation in bismuth under shock loading. Journal of Applied Physics, 45, 135–139.

Rosenberg, Z. (1984). Determination of the dynamic phase transitions in bismuth with in-material manganin gauges. Journal of Applied Physics, 56(10), 3328–3329.

Simonenko, V. A., Voloshin, N. P., Vladimirov, A. S., Nagibin, A. P., Nogin, V. P., Popov, V. A., Sal'nikov, V. A., & Shoidin, Y. A. (1985). Absolute measurements of shock compressibility of aluminum at pressures p > 1 TPa. Soviet Physics JETP, 61, 869–873.

Strand, O. T., Goosman, D. R., Martinez, C., Whitworth, T. L., & Kuhlow, W. W. (2006). A novel system for high-speed velocimetry using heterodyne techniques. Review of Scientific Instruments, 77, 083108.

Thiel, M. van. (1977). Compendium of shock wave data (Lawrence Livermore Laboratory Report No. UCRL-50108). Livermore, CA.

Trunin, R. F., Moiseev, B. N., Podurets, M. A., Simakov, G. V., & Sevast'yanov, A. G. (1993). Determination of the shock compressibility of iron at pressures up to 10 TPa (100 mbar). Soviet Physics JETP, 76, 1095–1098.

Trunin, R. F., Podurets, M. A., Moiseev, B. N., Simakov, G. V., & Popov, L. V. (1969). Relative compressibility of copper, cadmium and lead at high pressures. Soviet Physics JETP, 29, 630–631.

Trunin, R. F., Produrets, M. A., Popov, L. V., Zubarev, V. N., Bakanova, A. A., Ktitorov, V. M., Sevast'yanov, A. G., Simakov, G. V., & Dudoladov, I. P. (1992). Measurement of the compressibility of iron at 5.5 TPa. Soviet Physics JETP, 75, 777–780.

Zhernokletov, M. V., Zubarev, V. N., & Sutulov, Y. N. (1984). Porous specimen adiabats and solid copper expansion isentropes. Journal of Applied Mechanics and Technical Physics, 25, 107–110.